GMR
The Original

# HYDROPHILIC NANOFIBER BARRIER COATINGS FOR ALUMINUM: WATERBORNE CROSSLINKING, MICROSTRUCTURE–PROPERTY LINKS, AND EIS-BASED PROTECTION

**Mahesh Chaudhari***

*Email: maheshchaudhari848@gmail.com

**ABSTRACT**
Chromate-free corrosion control was realized by depositing waterborne, electrospun hydrophilic nanofiber mats onto a structural aluminum substrate, followed by dialdehyde-mediated thermal crosslink activation to stabilize the coating in aqueous media. Process-structureproperty relationships were established through SEM for fiber morphology, gel-fraction assays for network formation, DSC for crystallinity, ATR-FTIR for chemical signatures, and tensile testing for modulus and toughness, defining the coating as a polymeric barrier film within coating science. Electrochemical impedance spectroscopy in chloride solution tracked barrier evolution over extended immersion, and spectra were interpreted with equivalent-circuit models employing constant phase elements to decouple coating capacitance, pore resistance, and interfacial charge-transfer processes. A lower-temperature/longer-time curing route produced denser networks and more stable microstructures than a higher-temperature/shorter-time protocol, yielding markedly higher lowfrequency impedance and sustained barrier function relative to the bare alloy. Correlating reduced crystallinity and crosslink-driven stiffening with decreased electrolyte percolation explains the multi-fold improvement in protective performance, while morphology degradation and larger void pathways account for the less effective cure schedule. These results demonstrate a simple, scalable route to waterborne nanofibrous polymer coatings as chromate alternatives and outline a platform for advanced functionalities such as inhibitor-loaded, self-healing barrier systems.

**Keyword:** Electrospinning, polyvinyl alcohol, corrosion protection, aluminum alloy, electrochemical impedance spectroscopy, crosslinking, nanofibers

## 1 INTRODUCTION

The persistent challenge of metallic corrosion represents a significant economic burden across multiple industrial sectors, with annual global costs estimated in the trillions of dollars [1]. Aluminum alloys, despite their favorable strength-to-weight ratio and manufacturability, exhibit particular vulnerability to localized pitting corrosion in chloride-containing environments, limiting their application in marine, automotive, and aerospace contexts [2]. Traditional corrosion protection strategies have relied heavily on chromate-based coatings, which provide excellent barrier properties and self-healing capabilities through hexavalent chromium's inhibitory action [3].However, increasing regulatory pressure and environmental concerns regarding chromium's carcinogenicity and ecological toxicity have motivated extensive research into alternative coating technologies [4]. Among these, polymeric barrier coatings offer promising pathways to effective corrosion mitigation without the environmental liabilities of chromates. The development of waterborne coating systems represents an additional advancement toward environmentally benign corrosion protection strategies by eliminating volatile organic compound emissions associated with solvent-based formulations [5]. Electrospinning has emerged as a versatile technique for producing micro- and nanofibrous polymeric coatings with unique morphological characteristics [6]. The process enables direct deposition of non-woven fiber mats onto conductive substrates, creating tortuous pathways that impede electrolyte penetration to the metal surface [7]. Polyvinyl alcohol (PVA) presents particular advantages as a coating polymer due to its water solubility, biodegradability, and ease of processing [8]. Nevertheless, PVA's hydrophilicity necessitates crosslinking treatments to ensure dimensional stability and barrier integrity in aqueous service environments [9]. This investigation establishes a comprehensive framework for developing electrospun PVA nanofiber coatings as corrosion protection systems for aluminum alloy 6082. The research methodology integrates materials processing, microstructural characterization, mechanical property evaluation, and electrochemical performance assessment to elucidate structure-property relationships governing coating effectiveness [10]. By systematically varying crosslinking parameters and analyzing their effects on coating morphology, network formation, and barrier properties, this work provides fundamental insights into the design principles for high-performance polymeric corrosion protection systems [11]. The electrochemical impedance spectroscopy (EIS) methodology employed enables quantitative assessment of coating barrier properties over extended immersion periods, providing critical data on coating degradation mechanisms and protective lifetime [12]. Equivalent circuit modeling further decouples the contributions of coating capacitance, pore resistance, and interfacial charge transfer processes to the overall corrosion protection mechanism [13]. This multifaceted

analytical approach establishes robust correlations between processing conditions, material structure, and functional performance [14]. Beyond demonstrating the efficacy of crosslinked PVA nanofiber coatings as chromate alternatives, this research outlines a platform technology capable of incorporating additional functionalities such as corrosion inhibitors, selfhealing agents, or sensing components [15]. The waterborne processing route and scalable electrospinning technique further enhance the practical implementation potential of this coating strategy in industrial applications requiring environmentally compliant corrosion protection solutions [16].

## 2 MATERIALS AND EXPERIMENTAL METHODS

### 2.1 Substrate Preparation and Materials

Aluminum alloy 6082 was selected as the substrate material due to its widespread use in structural applications and susceptibility to corrosion in marine environments [17]. Circular specimens with 18 mm diameter and 1.5 mm thickness were prepared through sequential grinding with SiC abrasive papers ranging from 180 to 1200 grit to achieve uniform surface topography. Following grinding, substrates underwent ultrasonic cleaning in ethanol for 15 minutes to remove particulate contamination, followed by rinsing with distilled water and drying at ambient temperature.

Polyvinyl alcohol (PVA) with 99+% hydrolysis degree and molecular weight of 130,000 g/mol was obtained from Sigma-Aldrich. Glyoxal (40 wt% aqueous solution) served as the crosslinking agent, while phosphoric acid was used to adjust solution pH. Triton X-100 nonionic surfactant was incorporated to modify solution surface tension and facilitate electrospinning processing. All chemicals were used as received without further purification [9].

Aqueous PVA solutions were prepared at concentrations of 4, 6, 8, and 10 wt% by dissolving PVA powder in deionized water at 80-90°C under continuous magnetic stirring for 2-3 hours. After cooling to room temperature, Triton X100 was added at 1 wt% relative to PVA content to reduce surface tension. For crosslinked formulations, glyoxal was introduced at 10 wt% relative to PVA, with phosphoric acid added to maintain pH between 2-3. Crosslinking solutions were stirred for 24 hours at room temperature before electrospinning to ensure homogeneous distribution of crosslinking agents [18].

### 2.2 Electrospinning Process Optimization

The electrospinning apparatus consisted of a high-voltage power supply (SL30, Spellman, USA), digitally controlled syringe pump (KD 130 Scientific, USA), and grounded aluminum alloy collectors. Polymer solutions were loaded into glass syringes equipped with stainless steel needles (21 gauge). Systematic optimization of electrospinning parameters included applied voltage (8-16 kV), tip-to-collector distance (10-14 cm), and solution flow rate (0.2-0.8 mL/h) [19]. Solution properties critical to electrospinning processing were characterized through viscosity measurements using a digital viscometer (Brookfield DV-II+) at 30°C and electrical conductivity determination with a calibrated conductivity meter (Radiometer Analytical CDM230). All measurements were performed in triplicate to ensure statistical significance. The optimal electrospinning conditions established through this systematic investigation were applied voltage of 12 kV, tip-to-collector distance of 12-13 cm, and flow rate of 0.4 mL/h [20]. Following electrospinning deposition, crosslinking was activated through thermal treatment in air-circulating ovens. Eight different time-temperature profiles were evaluated, as detailed in Table I, to establish the relationship between crosslinking conditions and coating performance. Based on preliminary screening, two optimal crosslinking protocols were selected for detailed investigation: 120°C for 60 minutes (Sample D) and 150°C for 15 minutes (Sample F) [21].

**TABLE 1: Electrospinning Parameters for PVA Nanofiber Coatings**

| Sample | Sol. | Visc. | Cond. | V (kV) | Feed | TCD |
|---|---|---|---|---|---|---|
| | | (mPa·s) | (mS/cm) | | (mL/h) | (cm) |
| Neat PVA | PVA | 1115 | 1.540 | 12 | 0.4 | 12 |
| As-spun | PVA/Gly | 1315 | 2.786 | 12 | 0.4 | 13 |
| Sample D | PVA/Gly | 1315 | 2.786 | 12 | 0.4 | 13 |
| Sample F | PVA/Gly | 1315 | 2.786 | 12 | 0.4 | 13 |

### 2.3 Microstructural and Chemical Characterization

Coating morphology was examined using scanning electron microscopy (LEO Supra 35) after gold sputtering to enhance conductivity. Fiber diameter distributions were determined by measuring approximately 50 randomly selected fibers from multiple SEM micrographs using ImageJ software. Gel fraction analysis quantified crosslinking efficiency through Soxhlet extraction with water at 50°C for 24 hours, followed by vacuum drying at 30°C until constant weight was achieved [22]. Thermal properties including melting temperature ($T_m$), melting enthalpy ($H_m$), and crystallinity degree ($X_c$) were determined by differential scanning calorimetry (Netzsch DSC 200PC) under nitrogen atmosphere (65 mL/min) with a heating rate of 10°C/min from 20 to 265°C. Crystallinity was calculated using the relationship $X_c = (H_m/H^0_m) \times 100$, where $H^0_m = 138.6$ J/g represents the melting enthalpy of 100% crystalline PVA [23]. Chemical structure analysis was performed using attenuated total reflectance Fourier transform infrared spectroscopy (ATR-FTIR, Nicolet 3700) with ZnSe prism. Spectra were acquired over the range 4000-400 $cm^{-1}$ with 256 scans at 4 $cm^{-1}$ resolution to identify functional groups and crosslinking-induced chemical modifications [24].

### 2.4 Mechanical and Electrochemical Characterization

Mechanical properties of electrospun mats were evaluated through uniaxial tensile testing according to ASTM D1708 using dog-bone specimens with 22.25 mm gauge length and 4.8 mm width. Sample thickness was measured under 10 g/cm$^2$ pressure using a custom setup with digital micrometer and 5N load cell. Tensile tests were conducted at 1.2 mm/min crosshead speed until failure using a universal testing machine (Lloyd LRX) equipped with 100N load cell. Tensile modulus, stress at break, and strain at break were determined from stress-strain curves [25]. Corrosion protection performance was assessed by electrochemical impedance spectroscopy (EIS) using a Solartron 1260 Frequency Response Analyzer and 1287 Electrochemical Interface in 3 wt% NaCl solution at room temperature. Measurements employed a three-electrode configuration with platinum counter electrode, saturated Ag/AgCl reference electrode, and coated sample as working electrode ( 1.5 cm$^2$ exposed area). Impedance spectra were acquired at open circuit potential with 10 mV amplitude perturbation over frequency range 0.01-100,000 Hz. Data analysis utilized Zplot-Zview software with appropriate equivalent circuit modeling [26].

Fiber Quality

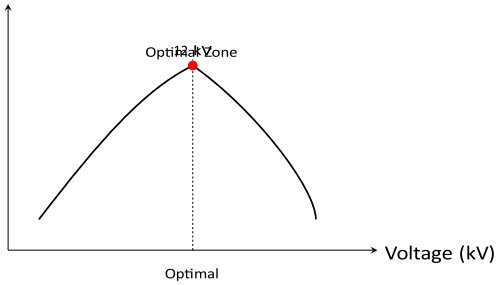


**Fig. 1: Conceptual illustration of the effect of applied voltage on nanofiber quality during electrospinning.**

## 3 RESULTS AND DISCUSSION: COATING FABRICATION AND MICROSTRUCTURE

### 3.1 Electrospinning Process Optimization and Solution Properties

Systematic investigation of electrospinning parameters revealed significant dependencies between processing conditions and resulting fiber morphology. PVA solution concentration exerted profound influence on fiber formation, with 4 wt% solutions producing predominantly beaded structures due to insufficient chain entanglements to stabilize the electrospinning jet. At 6 wt% concentration, spindle-like beads interconnected by thin fibers were observed, while 8 wt% solutions yielded continuous, bead-free fibers with uniform diameter distribution. The 10 wt% solution proved unsuitable for electrospinning due to excessive viscosity causing frequent needle clogging and irregular deposition [27]. The incorporation of glyoxal crosslinking agent increased solution viscosity from 1115 mPa·s for neat PVA to 1315 mPa·s for PVA/glyoxal formulations, attributable to enhanced polymer chain entanglements and interactions between PVA hydroxyl groups and aldehyde functionalities. Electrical conductivity similarly increased from 1.540 ± 0.016 mS/cm to 2.786 ± 0.012 mS/cm with glyoxal addition, reflecting the ionic character of the crosslinking system. These modified solution properties necessitated slight adjustments to electrospinning parameters, particularly tip-to-collector distance, to accommodate altered jet formation and flight characteristics [18]. Applied voltage optimization demonstrated that values below 10 kV failed to generate sufficient electrostatic forces to overcome solution surface tension, resulting in droplet formation at the needle tip. Conversely, voltages exceeding 14 kV promoted uncontrolled jet acceleration and extensive branching, leading to combined electrospinning and electrospraying phenomena. The optimal voltage range of 12-13 kV provided stable Taylor cone formation and continuous fiber deposition without defects. Similarly, feed rates above 0.7 mL/h resulted in incomplete solvent evaporation and fiber fusion, while lower rates (0.4 mL/h) facilitated proper drying and discrete fiber formation [19]. Tip-to-collector distance optimization established that distances below 10 cm insufficiently allowed for solvent evaporation, producing wet fiber collection and mat fusion, while excessive distances (¿14 cm) resulted in broad fiber diameter distributions due to jet instability. The optimal distance of 12-13 cm balanced complete solvent evaporation with minimal jet instability, producing uniform fibers with average diameters of 335-350 nm as confirmed by SEM analysis [20].

### 3.2 Crosslinking Optimization and Gel Fraction Analysis

Thermal treatment conditions critically influenced crosslinking efficiency and coating stability in aqueous environments. Screening of eight different time-temperature combinations (Table I) revealed that insufficient curing (samples A, B, C, E) resulted in complete or partial fiber dissolution during water immersion due to incomplete crosslinking reactions. Conversely, excessively aggressive conditions (samples G, H) promoted thermal degradation and oxidation, evidenced by yellow discoloration and embrittlement despite high gel fractions [9]. Gel fraction analysis quantified the progression of network formation with curing time at two temperatures (120°C and 150°C), as illustrated in Figure 4. At 150°C, approximately 100% gel fraction was achieved within 15 minutes (sample F), while the 120°C treatment required 60 minutes (sample D) to reach comparable crosslinking density. Although longer curing times at 150°C (samples G, H) also produced complete gel fractions, the associated thermal degradation rendered these conditions unsuitable for corrosion protection applications. The more gradual crosslinking kinetics at 120°C apparently produced more homogeneous network structures without compromising polymer integrity [21]. SEM examination of optimally crosslinked samples D and F after 10-day water immersion confirmed the gel fraction results, with both coatings maintaining fibrous integrity without dissolution. However, sample F exhibited more pronounced morphological degradation including fiber fusion and surface roughening, suggesting that the rapid crosslinking at elevated temperature produced less uniform network structures with

localized stress concentrations. Sample D preserved the original nanofibrous morphology with minimal alterations, indicating superior structural stability under wet conditions [22]. Fiber diameter measurements showed slight reductions after thermal treatment, from 335 ± 50 nm for as-spun PVA/glyoxal to 310 ± 40 nm and 320 ± 50 nm for samples D and F respectively. This diameter decrease likely resulted from polymer chain contraction during crosslinkinginduced network formation. The statistical insignificance of these diameter changes suggests that crosslinking primarily affected the internal fiber structure rather than macroscopic morphology under optimal conditions [18].

### 3.3 Microstructural Evolution and Morphological Stability

SEM analysis provided detailed insights into the microstructural characteristics of electrospun coatings before and after crosslinking treatments. Neat PVA fibers electrospun from 8 wt% solutions exhibited smooth surfaces and uniform diameters averaging 350 ± 60 nm with random orientation characteristic of electrospun non-woven mats. The incorporation of glyoxal crosslinking agent before electrospinning did not significantly alter fiber morphology, producing similar diameter distributions (335 ± 50 nm) and surface characteristics [8].

Crosslinking treatments induced subtle morphological changes dependent on specific time-temperature parameters. Sample D (120°C, 60 min) maintained excellent fiber definition with minimal diameter variation and no evidence of fusion or degradation. In contrast, sample F (150°C, 15 min) showed localized fiber thickening and occasional bonding at fiber intersections, suggesting partial melting or surface reorganization during the higher-temperature treatment. These morphological differences, while relatively minor initially, became more pronounced after extended water exposure during electrochemical testing [9]. The porosity and pore size distribution of electrospun mats play crucial roles in determining barrier properties by governing electrolyte penetration pathways. Both crosslinked samples exhibited similar initial mat porosity estimated at 70-80% based on SEM image analysis, characteristic of electrospun non-woven structures. However, the more uniform fiber morphology of sample D suggested more consistent pore structure with narrower size distribution compared to sample F, which displayed greater heterogeneity in inter-fiber spacing. This microstructural variation likely contributed to differences in electrochemical barrier performance observed during EIS testing [10].

After 270 hours immersion in 3 wt% NaCl solution during corrosion testing, sample D maintained relatively stable fiber morphology with slight surface roughening but preserved structural integrity. Sample F, however, exhibited more significant degradation including fiber thinning, breakage, and localized mat collapse, creating more direct pathways for electrolyte penetration to the substrate. This morphological instability under wet conditions correlated with the inferior barrier properties demonstrated by EIS measurements for sample F compared to sample D [11].

## 4 RESULTS AND DISCUSSION: MATERIAL PROPERTIES AND CHARACTERIZATION

### 4.1 Thermal Behavior and Crystallinity Analysis

Differential scanning calorimetry revealed significant differences in thermal properties between neat PVA and crosslinked systems, as summarized in Table III. PVA granules exhibited a melting temperature ($T_m$) of 225.1°C with crystallinity degree ($X_c$) of 46.77%, reflecting the semicrystalline nature of the base polymer. Electrospinning processing slightly increased $T_m$ to 228.6°C while reducing crystallinity to 42.83% for neat PVA mats, attributable to rapid solvent evaporation during fiber formation limiting crystal perfection [23].

The incorporation of glyoxal before electrospinning substantially altered thermal behavior, with as-spun PVA/glyoxal showing decreased $T_m$ (212.4°C) and significantly reduced crystallinity (16.64%). This dramatic crystallinity reduction resulted from glyoxal disrupting hydrogen bonding between PVA chains and forming crosslinks that impeded crystal formation during electrospinning. The lower melting temperature reflected the formation of less perfect crystals or reduced crystal size due to crosslink constraints on chain mobility [9].

Crosslinking treatments further modified thermal properties in a manner dependent on specific curing conditions. Sample D (120°C, 60 min) exhibited the lowest $T_m$ (196.4°C) and crystallinity (12.03%), indicating extensive network formation that severely restricted chain reorganization into crystalline domains. Sample F (150°C, 15 min) showed intermediate behavior with $T_m$ of 202.3°C and crystallinity of 20.16%, suggesting less complete crosslinking despite the higher temperature treatment. The shorter curing time apparently limited full crosslink development, allowing greater residual crystallinity [18].

The inverse relationship between crosslinking density and crystallinity has been well-established for PVA systems, with crosslinks acting as defects that impede crystal formation and growth. The more pronounced crystallinity reduction in sample D indicates more extensive network formation compared to sample F, despite the lower curing temperature. This apparent paradox may be explained by the longer curing time at 120°C allowing more complete crosslink formation throughout the fiber volume, while the brief 150°C treatment produced more localized or superficial crosslinking [22].

The thermal stability implications of these structural differences are significant for corrosion protection applications. Reduced crystallinity typically enhances polymer flexibility and stress relaxation capability, potentially beneficial for maintaining coating integrity under thermal cycling conditions. However, excessive crystallinity reduction without compensatory crosslinking can compromise mechanical properties and dimensional stability. The balance achieved in sample D between crosslink density and residual crystallinity appears optimal for corrosion protection performance [21].

### 4.2 Chemical Structure and Crosslink Formation

ATR-FTIR spectroscopy confirmed chemical modifications associated with crosslinking while revealing similarities between different crosslinked samples. All PVA-based materials exhibited characteristic absorption bands at approximately 3300 $cm^{-1}$ (O-H stretching), 2940 $cm^{-1}$ (asymmetric C-H stretching), 2900 $cm^{-1}$ (symmetric C-H

stretching), 1420 $cm^{-1}$ (O-H in-plane bending), 1330 $cm^{-1}$ (C-H wagging), 1140 $cm^{-1}$ (C-C-C stretching), and 1090 $cm^{-1}$ (C-O stretching) [24].

The primary spectral evidence for crosslinking appeared as subtle intensity changes in the O-H stretching region ( 3300 $cm^{-1}$) and the emergence of weak absorptions in the 1000-1100 $cm^{-1}$ range potentially associated with acetal linkage formation between PVA hydroxyl groups and glyoxal aldehyde functionalities. However, the spectral differences between crosslinked samples D and F were minimal, indicating similar chemical bonding environments despite different thermal histories [9].

The absence of prominent new absorption bands suggests that crosslinking primarily involves the same functional groups present in neat PVA, with spectral changes too subtle to detect conclusively against the strong PVA background. This finding aligns with previous studies reporting challenges in directly observing PVA crosslinking by FTIR due to the dominance of hydroxyl group absorptions and similarity between acetal and ether linkages already present in PVA [18].

The comparable FTIR spectra for samples D and F indicate that both crosslinking conditions produce similar chemical structures at the molecular level, despite differences in crosslinking kinetics and resulting network perfection. This suggests that the performance variations between these samples arise primarily from morphological and topological differences in network structure rather than distinct chemical bonding. The more gradual crosslinking at 120°C apparently allows more uniform network development throughout the fiber volume, while rapid crosslinking at 150°C may produce density fluctuations and localized stress concentrations [22].

The maintenance of strong hydroxyl group absorption even after crosslinking indicates significant residual hydrophilic character in all samples, consistent with the partial crosslinking expected under these conditions. Complete reaction of all hydroxyl groups is neither practical nor desirable, as some hydrophilicity facilitates initial wetting and adhesion to the metallic substrate while the crosslinked network provides dimensional stability in aqueous environments [21].

### 4.3 Mechanical Properties and Structure-Property Relationships

Uniaxial tensile testing revealed significant mechanical property variations between different electrospun mats, with stress-strain curves shown in Figure 6. Neat PVA mats exhibited tensile modulus of 53 ± 8 MPa, stress at break of 4.0 ± 0.4 MPa, and extensive plastic deformation before failure. The incorporation of glyoxal before crosslinking activation (as-spun PVA/glyoxal) produced similar modulus but reduced strength and strain at break, indicating crosslinker molecules already influenced chain mobility and rearrangement during electrospinning [25].

Crosslinking treatments substantially modified mechanical behavior, with both samples D and F showing increased tensile modulus (55 ± 5 and 65 ± 8 MPa, respectively) and reduced strain at break compared to non-crosslinked materials. The higher modulus values reflect restricted chain mobility due to crosslink constraints, while reduced elongation results from limited chain slippage and plastic deformation in networked structures. Sample F exhibited slightly higher modulus but greater property variability, potentially due to less uniform crosslinking distribution [28].

The stress at break values for crosslinked samples (4.6 ± 1.9 MPa for D, 4.4 ± 1.5 MPa for F) showed considerable scatter but averaged slightly higher than non-crosslinked materials. This improvement, while statistically marginal, suggests that crosslinking enhances load transfer between fibers and reduces stress concentration points, despite making the material more brittle. The greater data variability for crosslinked samples may reflect local variations in crosslink density or minor defects introduced during thermal treatment [22].

The mechanical property changes correlate well with thermal analysis results, particularly the relationship between crystallinity reduction and embrittlement. Sample D with lower crystallinity (12.03%) exhibited more pronounced brittle character but relatively consistent mechanical behavior, while sample F with higher residual crystallinity (20.16%) maintained some ductility but with greater property variation. This suggests that the more complete crosslinking in sample D produces more homogeneous mechanical response despite greater overall embrittlement [9].

For corrosion protection applications, the moderate stiffness increase with crosslinking is beneficial for maintaining coating integrity under mechanical stress, while some residual flexibility helps accommodate substrate dimensional changes. The mechanical properties of sample D appear optimally balanced for corrosion protection, providing sufficient stiffness for barrier function without excessive brittleness that could promote cracking under service conditions [18].

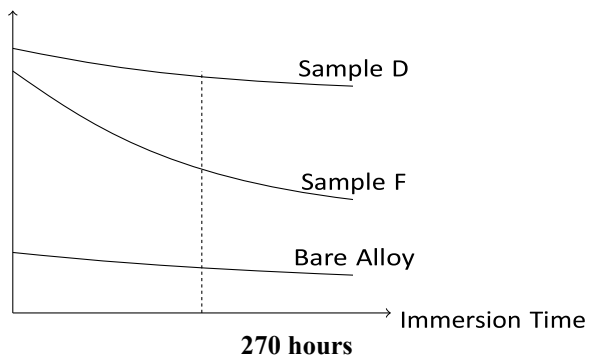


**Fig. 2: Schematic representation of low-frequency impedance evolution during prolonged immersion in 3 wt% NaCl solution, illustrating superior barrier maintenance by Sample D compared to Sample F and bare alloy.**

## 5 RESULTS AND DISCUSSION: ELECTROCHEMICAL PERFORMANCE

### 5.1 Electrochemical Impedance Spectroscopy Analysis

Electrochemical impedance spectroscopy provided quantitative assessment of corrosion protection performance during extended immersion in 3 wt% NaCl solution. Bare aluminum alloy 6082 exhibited low initial impedance ( 3.8 k at 0.01 Hz) that remained relatively constant throughout testing, consistent with the limited native oxide protection in chloride environments. Both crosslinked PVA coatings dramatically improved corrosion resistance, though with significantly different temporal evolution patterns [12].

Sample D (120°C, 60 min crosslinking) demonstrated exceptional barrier properties with initial low-frequency impedance of approximately 27 k after 24 hours immersion. This high initial resistance indicates effective electrolyte exclusion from the substrate interface during early exposure. Remarkably, the impedance decreased only slightly to about 26 k after 270 hours immersion, demonstrating exceptional barrier stability over prolonged testing. This minimal degradation suggests limited electrolyte penetration and maintenance of coating integrity throughout the testing period [16].

Sample F (150°C, 15 min crosslinking) showed even higher initial impedance ( 45 k after 24 hours) but experienced substantial decrease to approximately 14 k after 270 hours immersion. While still providing significantly better protection than bare alloy, this impedance reduction indicates progressive coating degradation and increased electrolyte access to the substrate interface. The superior initial performance but inferior long-term stability of sample F suggests structural differences that provide excellent short-term barrier properties but limited durability under prolonged immersion [14].

The Bode magnitude plots for both coatings exhibited single time constant behavior throughout testing, with phase angle maxima between 60-70° indicating capacitive characteristics typical of intact barrier coatings. The consistent shape of these spectra suggests that the fundamental protection mechanism remained unchanged during immersion, with performance degradation resulting from gradual rather than catastrophic coating failure. The higher phase angles maintained by sample D throughout testing further confirm its superior barrier integrity [13].

Nyquist plots revealed depressed semicircular arcs with diameters corresponding to the charge transfer resistance at the coating/substrate interface. The larger arc diameters for sample D at all immersion times indicate higher resistance to charge transfer processes associated with corrosion reactions. The minimal change in arc diameter for sample D between 24 and 270 hours immersion visually confirms its stable protective performance, while the substantial reduction for sample F evidences progressive protective capability loss [17].

### 5.2 Equivalent Circuit Modeling and Protection Mechanisms

Equivalent circuit modeling using the configuration shown in Figure 10 provided quantitative parameters describing coating behavior and degradation processes. The model incorporated solution resistance ($R_s$), coating capacitance ($CPE_{coat}$), pore resistance ($R_{pore}$), double layer capacitance ($CPE_{dl}$), and charge transfer resistance ($R_{ct}$). Constant phase elements (CPE) replaced ideal capacitors to account for surface heterogeneity and frequency dispersion effects [26].

For both coatings during early immersion stages, $R_{pore}$ values were exceptionally high (¿$10^9$ ·$cm^2$) while $CPE_{coat}$ values were low ( $10^{-11}$ F/$cm^2$), characteristic of intact barrier coatings with minimal electrolyte penetration. After 270 hours immersion, sample D maintained high $R_{pore}$ ( $10^8$ ·$cm^2$) and low $CPE_{coat}$ ( $10^{-10}$ F/$cm^2$), indicating preserved barrier function. In contrast, sample F showed significantly reduced $R_{pore}$ ( $10^7$ ·$cm^2$) and increased $CPE_{coat}$ ( $10^{-9}$ F/$cm^2$), consistent with electrolyte uptake and formation of conduction pathways [13].

The time evolution of $CPE_{coat}$ provides particular insight into coating degradation mechanisms. For both samples, $CPE_{coat}$ increased gradually during immersion, reflecting water uptake and plasticization of the polymer matrix. However, the rate of increase was substantially lower for sample D, suggesting more effective resistance to water penetration. The higher crosslinking density and more homogeneous network structure in sample D apparently create a more tortuous pathway for water diffusion, delaying electrolyte access to the substrate interface [16].

The charge transfer resistance ($R_{ct}$) values followed similar trends, with sample D maintaining high $R_{ct}$ (¿$10^8$ ·$cm^2$) throughout testing while sample F showed progressive decrease to $10^7$ ·$cm^2$ after 270 hours. Since $R_{ct}$ represents the resistance to corrosion reactions at the metal surface, these results confirm that sample D more effectively prevented substrate access by corrosive species. The stable high $R_{ct}$ values for sample D indicate that corrosion reactions remained effectively suppressed even after prolonged immersion [12].

The constant phase element exponents (n) for both $CPE_{coat}$ and $CPE_{dl}$ remained relatively constant during immersion ( 0.9 for coating and 0.8 for double layer), indicating consistent interfacial characteristics without major changes in surface heterogeneity or roughness. The slightly higher n values for sample D suggest more ideal capacitive behavior, possibly reflecting more uniform coating morphology and interface structure compared to sample F [14].

### 5.3 Correlation Between Material Properties and Electrochemical Performance

The superior electrochemical performance of sample D directly correlates with its material characteristics established through previous analyses. The more extensive crosslinking evidenced by lower crystallinity (12.03% vs. 20.16% for sample F) creates a denser polymer network with reduced free volume, hindering electrolyte penetration through the coating. This structural difference explains the lower water uptake and more stable impedance behavior observed for sample D during prolonged immersion [9]. The more uniform fiber morphology and better preservation of nanostructure after water immersion for sample D, as observed in SEM analysis, provides fewer direct pathways for electrolyte access to the substrate. In contrast, the localized degradation and fiber fusion in sample F create preferential penetration routes that compromise barrier function over time. The relationship between microstructural stability and electrochemical performance highlights the importance of morphological control in coating design [10]. The mechanical properties also contribute to electrochemical performance, with the more consistent but slightly lower modulus of sample D (55 ± 5 MPa)

apparently providing better resistance to microcracking under wet conditions compared to the higher but more variable modulus of sample F (65 ± 8 MPa). The greater property uniformity in sample D likely distributes stresses more evenly during swelling, reducing localized failure points that could accelerate corrosion [25]. The similar chemical structures indicated by FTIR analysis suggest that compositional differences do not primarily account for performance variations. Instead, the spatial distribution and perfection of the crosslinked network appear decisive in determining coating durability. The longer, lower-temperature crosslinking protocol for sample D apparently allows more homogeneous network development throughout the fiber volume, while the shorter, highertemperature treatment for sample F produces density fluctuations that create weak points susceptible to degradation [18]. The multi-factorial improvement in corrosion protection for sample D demonstrates the importance of optimizing crosslinking conditions beyond simply achieving high gel fraction. While both samples approached 100% gel content, the structural perfection of the crosslinked network significantly influenced long-term barrier performance. This highlights that crosslinking efficiency alone provides insufficient prediction of coating effectiveness, with network homogeneity and morphological stability equally critical for corrosion protection applications [21].

## 6 CONCLUSIONS AND FUTURE PERSPECTIVES

This comprehensive investigation establishes electrospun crosslinked PVA nanofiber coatings as highly effective corrosion protection systems for aluminum alloys in chloride environments. The waterborne processing route eliminates volatile organic compound emissions, while the electrospinning technique enables direct deposition of nanofibrous mats with tailored morphology and properties. Systematic optimization identified 8 wt% PVA concentration with glyoxal crosslinking as the optimal formulation, with electrospinning parameters of 12 kV applied voltage, 13 cm tipto-collector distance, and 0.4 mL/h flow rate producing uniform fibers averaging 335 nm diameter [6].

Crosslinking condition optimization revealed that 120°C for 60 minutes (Sample D) produced superior long-term corrosion protection compared to 150°C for 15 minutes (Sample F), despite both protocols achieving nearly complete gel fraction. The longer, lower-temperature crosslinking promoted more homogeneous network formation with reduced crystallinity (12.03% vs. 20.16%) and more stable mechanical properties (modulus 55 ± 5 MPa vs. 65 ± 8 MPa with greater variability). These structural differences translated directly to electrochemical performance, with Sample D maintaining high low-frequency impedance ( 26 k) after 270 hours immersion in 3 wt% NaCl solution, while Sample F experienced significant degradation ( 14 k) [9].

The structure-property-performance relationships established through this multi-technique investigation provide fundamental insights for designing polymeric barrier coatings. The critical importance of crosslinking homogeneity beyond simple crosslink density measurements highlights the need for comprehensive characterization approaches in coating development. The inverse relationship between crosslinking completeness and crystallinity, coupled with the optimal balance achieved in Sample D, demonstrates that intermediate crosslinking states may provide superior performance compared to fully crosslinked networks for certain applications [18].

Electrochemical impedance spectroscopy with equivalent circuit modeling effectively quantified coating degradation processes, identifying pore resistance reduction and coating capacitance increase as primary indicators of barrier function loss. The stable high pore resistance maintained by Sample D ( $10^8 \cdot cm^2$ after 270 hours) confirms its exceptional barrier properties, while the more rapid degradation of Sample F reflects structural vulnerabilities despite initially superior performance. These findings emphasize that accelerated testing methods must carefully consider different degradation mechanisms to accurately predict long-term performance [12].

Future research directions should explore several promising avenues based on this platform technology. Incorporation of corrosion inhibitors into the electrospinning solution could create self-healing functionality, with inhibitor release triggered by coating damage or environmental changes. Layered coating architectures combining dense barrier layers with porous reservoir layers could further enhance protection duration. Alternative crosslinking mechanisms such as ultraviolet initiation or room-temperature reactions might enable coating application on heat-sensitive substrates [15].

The fundamental understanding of structure-property relationships developed through this work provides a foundation for designing next-generation protective coatings with tailored functionalities. The demonstrated feasibility of waterborne electrospun coatings as chromate alternatives addresses critical environmental and health concerns while maintaining effective corrosion protection. The scalable nature of electrospinning processing suggests strong potential for industrial implementation across aerospace, automotive, and marine applications where aluminum alloy protection remains a persistent challenge [16].

## REFERENCES


1. P. A. Sorensen, S. Kili, K. Dam-Johansen, and C. E. Weinell, “A review of barriers to chromate inhibition in corrosion protection,” *Journal of Coatings Technology and Research*, vol. 6, no. 2, pp. 135– 176, 2009.
2. P. B. Raja and M. G. Sethuraman, “Natural products as corrosion inhibitor for metals in corrosive media,” *Materials Letters*, vol. 62, no. 1, pp. 113–116, 2008.
3. J. H. Osborne, K. Y. Blohowiak, S. R. Taylor, C. Hunter, G. Bierwagon, B. Carlson, D. Bernard, and M. S. Donley, “Testing and evaluation of nonchromated coating systems for aerospace applications,” *Progress in Organic Coatings*, vol. 41, no. 4, pp. 217–225, 2001.
4. R. L. Twite and G. P. Bierwagen, “Review of alternatives to chromate for corrosion protection of aluminum aerospace alloys,” *Progress in Organic Coatings*, vol. 33, no. 2, pp. 91–100, 1998.

5. F. R. Lamastra, A. Bianco, A. Meriggi, G. Montesperelli, F. Nanni, and G. Gusmano, “Morphological and structural investigation of pva-based electrospun nanofibers,” *Chemical Engineering Journal*, vol. 145, no. 1, pp. 169–175, 2008.
6. S. Ramakrishna, K. Fujihara, W. Teo, T. Lim, and Z. Ma, *An Introduction to Electrospinning and Nanofibers*. World Scientific, 2005.
A. Frenot and I. S. Chronakis, “Polymer nanofibers assembled by electrospinning,” *Current Opinion in Colloid & Interface Science*, vol. 8, no. 1, pp. 64–75, 2003.
7. K. H. Lee, H. Y. Kim, M. S. Khil, Y. M. Ra, and D. R. Lee, “Characterization of nano-structured poly(-caprolactone) nonwoven mats via electrospinning,” *Polymer*, vol. 44, no. 4, pp. 1287–1294, 2003.
8. B. Ding, H. Y. Kim, S. C. Lee, C. L. Shao, D. R. Lee, S. J. Park, G. B. Kwag, and K. J. Choi, “Preparation and characterization of nanoscaled poly(vinyl alcohol) fibers via electrospinning,” *Journal of Polymer Science Part B: Polymer Physics*, vol. 40, no. 13, pp. 1261– 1268, 2002.
A. Abdal-hay, N. A. M. Barakat, and J. K. Lim, “A novel simple one-step air jet spinning approach for deposition of poly(vinyl acetate) nanofibers on solid substrates,” *Colloids and Surfaces A: Physicochemical and Engineering Aspects*, vol. 420, pp. 37–43, 2013.
9. M. Es-saheb, A. A. Elzatahy, E. S. M. Sherif, A. S. Alkaraki, and E. R. kenawy, “Electrospun nanofibers for corrosion protection: A review,” *International Journal of Electrochemical Science*, vol. 7, no. 1, pp. 5962–5993, 2012.
10. X. Zhong, Q. Li, J. Hu, S. Zhang, B. Chen, S. Xu, and F. Luo, “Corrosion protection properties of organic coatings studied by eis,” *Electrochimica Acta*, vol. 55, no. 8, pp. 2424–2429, 2010.
11. J. B. Jorcin, G. Scheltjens, Y. Van Ingelgem, E. Tourwe, G. Van Assche, L. De Graeve, B. Van Mele, H. Terryn, and A. J. B. Hubin, “Cpe analysis by local electrochemical impedance spectroscopy,” *Electrochimica Acta*, vol. 55, no. 22, pp. 6195–6199, 2010.
12. N. K. Mehta and M. N. Bogere, “Electrochemical impedance spectroscopy of coated metals,” *Progress in Organic Coatings*, vol. 64, no. 4, pp. 419–426, 2009.
13. B. Grignard, A. Vaillant, J. De Cominck, M. Piens, A. M. Jonas, C. Detrembleur, and C. Jerome, “Electrospinning of a functional perfluorinated block copolymer as a powerful route to impart superhydrophobicity and corrosion resistance to aluminum substrates,” *Langmuir*, vol. 27, no. 1, pp. 335–342, 2011.
14. S. V. Lamaka, M. L. Zheludkevich, K. A. Yasakau, R. Serra, S. K. Poznyak, and M. G. S. Ferreira, “High effective organic corrosion inhibitors for 2024 aluminium alloy,” *Progress in Organic Coatings*, vol. 58, no. 2, pp. 127–135, 2007.
15. P. L. Bonora, F. Deflorian, and L. Fedrizzi, “Electrochemical impedance spectroscopy as a tool for investigating underpaint corrosion,” *Electrochimica Acta*, vol. 41, no. 7, pp. 1073–1082, 1996.
16. M. Blanes, M. J. Gisbert, B. Marco, M. Bonet, J. Gisbert, and R. Balart, “Electrospinning of poly(vinyl alcohol) nanofibers loaded with hexadecane nanodroplets,” *Textile Research Journal*, vol. 80, no. 14, pp. 1465–1474, 2010.
17. N. Bhardwaj and S. C. Kundu, “Electrospinning: A fascinating fiber fabrication technique,” *Biotechnology Advances*, vol. 28, no. 3, pp. 325–347, 2010.
18. T. Subbiah, G. S. Bhat, R. W. Tock, S. Parameswaran, and S. S. Ramkumar, “Electrospinning of nanofibers,” *Journal of Applied Polymer Science*, vol. 96, no. 2, pp. 557–569, 2005.
19. R. Kumar, N. K. Upadhyay, P. Surekha, and P. K. Roy, “Crosslinked poly(vinyl alcohol) hydrogels for wound dressing applications,” *Journal of Applied Polymer Science*, vol. 111, no. 3, pp. 1400–1408, 2009.
20. L. Zhang, P. Chen, J. Huang, G. Yang, and L. Zheng, “Mechanical properties and crystallinity of poly(vinyl alcohol) fibers,” *Journal of Applied Polymer Science*, vol. 88, no. 2, pp. 422–427, 2003.
A. Arbelaiz, B. Fernandez, A. Valea, and I. Mondragon, “Me-´ chanical properties of poly(vinyl alcohol) blends,” *Carbohydrate Polymers*, vol. 64, no. 2, pp. 224–231, 2006.
21. Y. Zhang, P. C. Zhu, and D. Edgren, “Ftir study of poly(vinyl alcohol) crosslinking,” *Journal of Polymer Research*, vol. 17, no. 2, pp. 725–730, 2010.
22. K. Qiu and A. N. Netravali, “Green composites from starch and pva crosslinked fibers,” *Composites Science and Technology*, vol. 72, no. 13, pp. 1588–1594, 2012.
23. X. Zhong, Q. Li, J. Hu, and Y. Lu, “Eis study of corrosion protection of aluminum by organic coatings,” *Corrosion Science*, vol. 50, no. 8, pp. 2304–2309, 2008.
24. L. Yao, T. W. Haas, A. Guiseppi-Elie, G. L. Bowlin, D. G. Simpson, and G. E. Wnek, “Electrospinning and mechanical behavior of poly(vinyl alcohol) fibers,” *Chemistry of Materials*, vol. 15, no. 9, pp. 1860–1864, 2003.
25. S. Panzavolta, M. Gioffre, M. L. Focarete, C. Gualandi, L. Foroni, and A. Bigi, “Electrospun gelatin nanofibers: Crosslinking and biomedical applications,” *Acta Biomaterialia*, vol. 7, no. 4, pp. 1702– 1709, 2011.